GEOPHYSICS, VOL. 86, NO. 3 (MAY-JUNE 2021); P. T143–T154, 11 FIGS., 3 TABLES.
10.1190/GEO2020-0296.1

An optimal frequency-domain finite-difference operator with a flexible stencil and its application in discontinuous-grid modeling

Na Fan[1], Xiao-Bi Xie[2], Lian-Feng Zhao[3], Xin-Gong Tang[1], and Zhen-Xing Yao[3]

ABSTRACT

We have developed an optimal method to determine expansion parameters for flexible stencils in 2D scalar-wave finite-difference frequency-domain (FDFD) simulation. Our stencil only requires the involved grid points to be paired and rotationally symmetric around the central point. We apply this method to the transition zone in discontinuous-grid modeling, in which the key issue is designing particular FDFD stencils to correctly propagate the wavefield passing through the discontinuous interface. Our method can work in an FDFD discontinuous grid with arbitrary integer coarse- to fine-grid spacing ratios. Numerical examples are developed to determine how to apply this optimal method to discontinuous-grid FDFD schemes with spacing ratios of 3 and 5. The synthetic wavefields are highly consistent to those calculated using the conventional dense uniform grid, and the memory requirement and computational costs are greatly reduced. For velocity models with large contrasts, our discontinuous-grid FDFD method can significantly improve the computational efficiency in forward modeling, imaging, and full-waveform inversion.

INTRODUCTION

Full-waveform inversion (FWI) is considered to be a promising technique for retrieving the subsurface velocity structure. It heavily relies on forward modeling during iterations in the optimization process. The modeling can be performed either in the frequency or time domain. Frequency-domain FWI becomes attractive because it can be naturally built into multiscale approaches to mitigate cycle skipping, conveniently handle independent frequencies and multishot computations, or easily include the frequency-dependent attenuation. Another advantage is that the frequency-domain method does not need to store wavefield values when calculating the gradient (Vigh and Starr, 2008; Virieux and Operto, 2009). Frequency-domain finite-difference (FDFD) forward modeling is an important part of frequency-domain FWI. Great efforts have been made to develop optimal FDFD operators. Jo et al. (1996) propose an optimal nine-point scheme based on rotated FDFD operators. Succeeding researchers extended this idea to other FDFD schemes, such as acoustic 25- and 17-point schemes, and certain elastic and viscoelastic applications (e.g., Shin and Sohn, 1998; Štekl and Pratt, 1998; Hustedt et al., 2004; Operto et al., 2007, 2009, 2014; Cao and Chen, 2012). Min et al. (2000) propose the weighted-average method to simplify the optimal procedure of Jo et al. (1996), which was later applied to other cases (e.g., Gu et al., 2013; Yang and Mao, 2016). Targeted to cases with different vertical and horizontal spacings, Chen (2012) proposes a new optimal nine-point scheme based on the average-derivative method (ADM), and it has been extended to other cases (e.g., Tang et al., 2015; Zhang et al., 2015; Chen and Cao, 2016, 2018). However, these optimized operators cannot be easily expanded from the commonly used nine-point scheme to other schemes with different FDFD stencils. Therefore, similar to the finite-difference time-domain (FDTD) optimization operators (Holberg, 1987; Etgen, 2007; Wang et al., 2019a), a general optimized FDFD operator was proposed by Fan et al. (2017) based on solving the frequency-domain 2D scalar-wave equation. Most previous FDFD schemes can be treated as special cases under this framework. In addition, applications of this optimal procedure have been extended to more complicated cases such as the 3D acoustic (Fan et al., 2018b) and elastic wave equations (Li et al., 2018).

FDFD is a computationally and memory intensive method (Plessix, 2009), which prevents it from being widely used in FWI.

Manuscript received by the Editor 22 May 2020; revised manuscript received 8 January 2021; published ahead of production 28 January 2021; published online 19 March 2021.
[1]Yangtze University, Key Laboratory of Exploration Technology for Oil and Gas Resources of Ministry of Education, Wuhan 430100, China and Cooperative Innovation Center of Unconventional Oil and Gas (Ministry of Education & Hubei Province), Wuhan, China. E-mail: fannachina@hotmail.com (corresponding author); tangxg@yangtzeu.edu.cn.
[2]University of California at Santa Cruz, Institute of Geophysics and Planetary Physics, Santa Cruz, California 95064, USA. E-mail: xxie@ucsc.edu.
[3]Chinese Academy of Sciences, Key Laboratory of Earth and Planetary Physics, Institute of Geology and Geophysics, Beijing 100864, China. E-mail: zhaolf@mail.iggcas.ac.cn; yaozx@mail.iggcas.ac.cn.

DOI:10.1190/geo2020-0296.1

The nonuniform-grid method, which usually uses variable grid density to discretize models with large velocity contrasts, was developed to mitigate this disadvantage (Wang et al., 2019c). The nonuniform-grid finite-difference (FD) modeling algorithms can be classified into two groups. The first group uses continuous nonuniform grids that vary continuously along certain coordinates (Moczo, 1989; Falk et al., 1996; Opršal and Zahradník, 1999; Pitarka, 1999; Oliveira, 2003; Chu and Stoffa, 2012). The computation is usually very convenient once the FD operator can be applied to the rectangular grid. The second group uses discontinuous nonuniform grids that are flexible in terms of discretizing the model (Aoi and Fujiwara, 1999; Kristek et al., 2010; Zhang et al., 2013). This usually can save more computational costs, but it requires special treatment in the fine- to coarse-grid transition area (Jastram and Behle, 1992; Jastram and Tessmer, 1994; Wang et al., 2001; Fan et al., 2015). Similar nonuniform-grid techniques have been widely used in FDTD modeling (e.g., Kang and Baag, 2004; Huang and Dong, 2009a, 2009b; Liu et al., 2014; Fan et al., 2015; Nie et al., 2015; Wang et al., 2019c). For nonuniform-grid FDFD modeling, Li and Jia (2018) develop continuous-grid FDFD modeling method based on the ADM FDFD operator of Chen (2012). However, compared to continuous-nonuniform-grid FDFD modeling, the discontinuous-nonuniform-grid method can discretize the model more flexibly and further reduce costs. The major issue is in the fine-coarse grid transition zone, in which special FDFD operators need be designed to maintain the global accuracy of the wave propagation. By using Fan et al.'s (2017) general FDFD optimal procedure, Fan et al. (2018a) propose a discontinuous-grid FDFD method to transfer the wavefield across the fine-to-coarse transition zone without reducing accuracy. But the spacing ratio (N) was restricted to a power of two, which limited its practical applications.

In the following study, we develop a new optimal method with a flexible stencil for 2D scalar-wave FDFD and apply it to discontinuous-grid modeling. Theoretically, with the new method, the coarse-to-fine spacing ratio N can be expanded to any integer. In the rest part of this paper, we first introduce the optimal theory for discontinuous-grid FDFD schemes and we investigate their dispersion relations and the structures of the impedance matrices. Then, we validate the proposed method using numerical examples in discontinuous grids and their results are compared with those using the traditional uniform grid. Finally, a brief conclusion summarizes the advantages of the proposed method.

METHODOLOGY

FDFD operator

The frequency-domain 2D scalar wave equation can be expressed as (Jo et al., 1996)

$$\frac{\partial^2 P}{\partial x^2}+\frac{\partial^2 P}{\partial z^2}+\frac{\omega^2}{v^2}P=0, \tag{1}$$

where v is the model velocity, ω is the angular frequency, P is the pressure, and x and z are the horizontal and vertical spatial coordinates, respectively. To introduce a flexible FDFD stencil, we use the grid geometry shown in Figure 1, in which Figure 1a is a general stencil and Figure 1b and 1c are two sample stencils. The involved grid points have to be paired and centrosymmetric. In other words, every grid point is the same as another one located at 180° in rotation. Therefore, we only need to determine half of these points. For the general FDFD stencil in Figure 1a, the commonly used 9- or 25-point scheme can be considered as its special case. Similarly, we can form other stencils by choosing certain points from the general stencil or, equivalently, setting weighting coefficients to points of the general stencil (including using zero coefficients to eliminate unwanted points) to form new stencils such as in Figure 1b and 1c. Therefore, we can unify our analyses to specific stencils by investigating the general stencil. We use the general FDFD stencil in Figure 1a to approximate the two second-order spatial derivatives $\partial^2 P/\partial x^2$ and $\partial^2 P/\partial z^2$ in equation 1. For the mass acceleration term $\omega^2/v^2 P$, we follow the previous approaches (Jo et al., 1996; Min et al., 2000; Chen, 2012; Fan et al., 2017) and approximate it using the weighted sum of all grid points involved in the stencil and obtain

$$\begin{aligned}&\frac{1}{\Delta x^2}\sum_{j=0}^{N_z}\sum_{i=F(j)}^{N_x} c_{i,j}(P_{m+i,n+j}+P_{m-i,n-j})\\&+\frac{1}{\Delta z^2}\sum_{j=0}^{N_z}\sum_{i=F(j)}^{N_x} d_{i,j}(P_{m+i,n+j}+P_{m-i,n-j})\\&+\frac{\omega^2}{v^2}\sum_{j=0}^{N_z}\sum_{i=F(j)}^{N_x} b_{i,j}(P_{m+i,n+j}+P_{m-i,n-j})=0,\end{aligned} \tag{2}$$

where $P_{m,n}=P(m\Delta x, n\Delta z)$ and Δx and Δz are the horizontal and vertical sampling intervals, respectively. Subscripts i, j denote the spatial locations in Figure 1a, and

$$F(j)=\begin{cases}0, & \text{if } j=0\\ -N_x, & \text{if } j\neq 0\end{cases}. \tag{3}$$

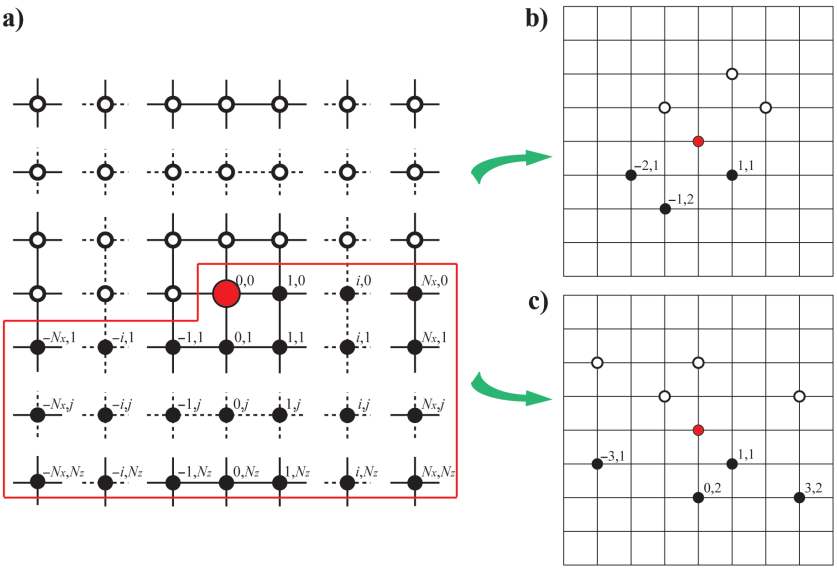

Figure 1. Schematic of the 2D FDFD schemes, in which (a) is the general stencil and (b and c) are two sample stencils. The locations circled by the red line are included in the summation.

The summation includes half of all the grid points as circled by the red line in Figure 1a. The terms $b_{i,j}$, $c_{i,j}$, and $d_{i,j}$ are the weighting coefficients for the mass acceleration term and two spatial derivatives, and they satisfy $\sum_{j=0}^{N_z}\sum_{i=F(j)}^{N_x} b_{i,j} = 1/2$ with $b_{i,j} \geq 0$, $\sum_{j=0}^{N_z}\sum_{i=F(j)}^{N_x} c_{i,j} = 0$, and $\sum_{j=0}^{N_z}\sum_{i=F(j)}^{N_x} d_{i,j} = 0$, respectively. When we set Nx = 1, $Nz = 1$, it becomes the commonly used 9-point scheme, and when $Nx = 2$, $Nz = 2$, it is the 25-point scheme. Other 2D FDFD schemes can also be considered as its special cases.

Similar to Fan et al. (2017), we separate the analysis of $\Delta x \geq \Delta z$ from $\Delta x < \Delta z$. Only the former will be investigated, and the latter can be analyzed by exchanging the x- and z-directions. To simplify equation 2, we define $a_{i,j} = c_{i,j} + r^2 d_{i,j}$, where $r = \Delta x/\Delta z$ is the aspect ratio. By substituting them into equation 2, we obtain

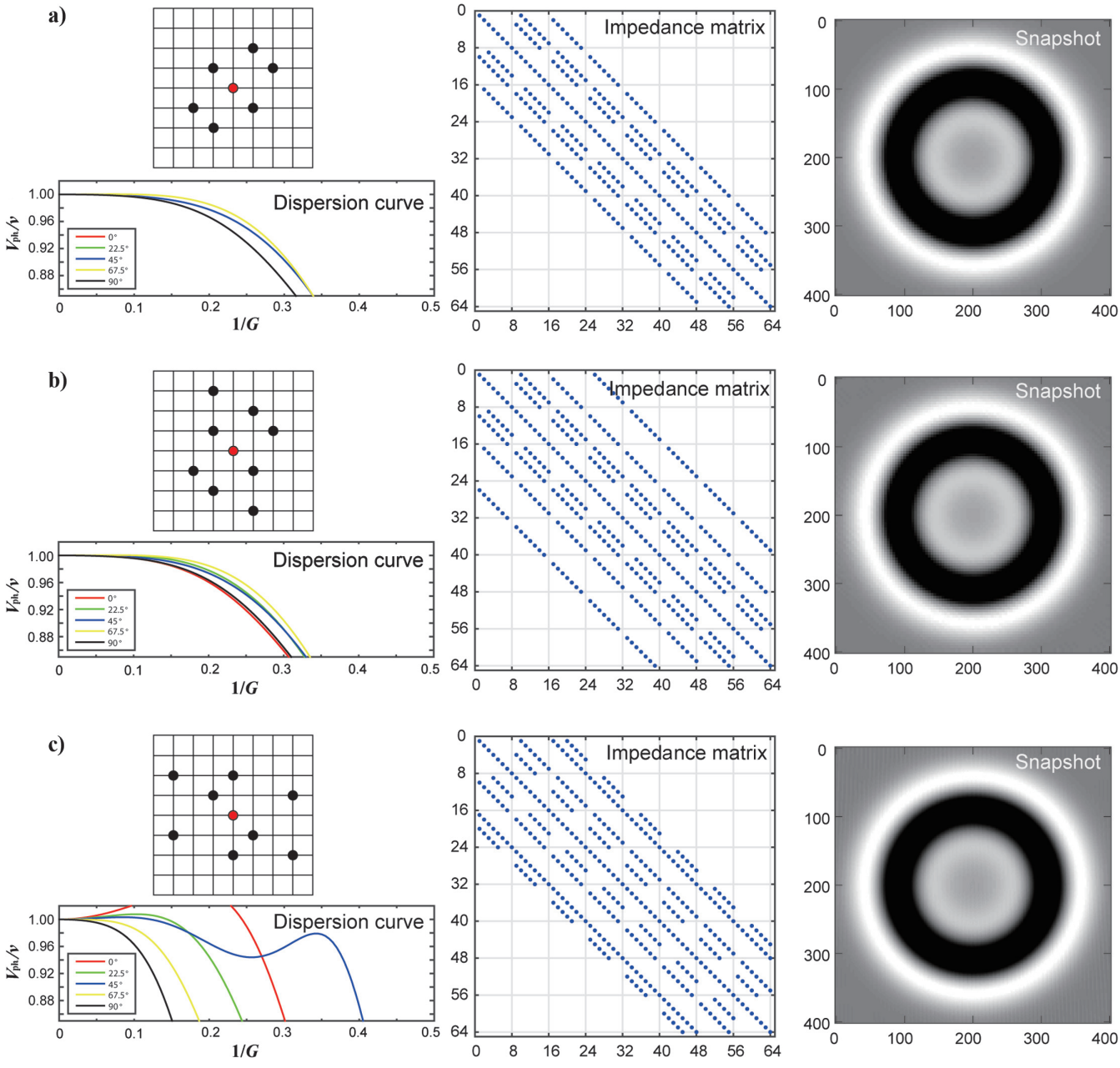

Figure 2. Comparison of three sample FDFD stencils. The three rows from top to bottom (a-c) are for different cases, in which the geometries of the stencils, dispersion curves, structures of impedance matrices, and synthetic snapshots are presented. Dispersion curves of different colors denote different propagation angles. The calculation of the impedance matrix is based on a small 8 × 8 grid model. The simulation is based on the same 2D homogeneous medium with a velocity of 3500 m/s, and a 30 Hz Ricker wavelet is used as the source. The spatial interval is 4 m for the schemes in (a and b), but it is 2 m for the scheme in (c) because of its lower accuracy.

$$\frac{1}{\Delta x^2}\sum_{j=0}^{N_z}\sum_{i=F(j)}^{N_x} a_{i,j}(P_{m+i,n+j}+P_{m-i,n-j}) + \frac{\omega^2}{v^2}\sum_{j=0}^{N_z}\sum_{i=F(j)}^{N_x} b_{i,j}(P_{m+i,n+j}+P_{m-i,n-j}) = 0, \quad (4)$$

where $a_{i,j}$ satisfies $\sum_{j=0}^{N_z}\sum_{i=F(j)}^{N_x} a_{i,j} = 0$.

Then, the classic dispersion analysis is implemented to obtain the optimization coefficients (Chen, 2012; Fan et al., 2017). We substitute a monochromatic plane wave $P(x,z,\omega) = P_0 e^{-i(k_x x + k_z z - \omega t)}$ into equation 4, where k_x and k_z are the horizontal and vertical components of the wavenumber vector, respectively, and we derive the normalized phase velocity V_{ph}/v as follows:

$$\frac{V_{\mathrm{ph}}}{v} = \frac{G}{2\pi}\sqrt{-\frac{\sum_{j=0}^{N_z}\sum_{i=F(j)}^{N_x} a_{i,j}T_{i,j}}{\sum_{j=0}^{N_z}\sum_{i=F(j)}^{N_x} b_{i,j}T_{i,j}}}, \quad (5)$$

where G is the number of grid points per wavelength, which is defined with respect to the larger spatial interval, $T_{i,j} = \cos(i(2\pi \sin\theta/G) + j(2\pi \cos\theta/rG))$, and θ is the propagation angle relative to the vertical axis. Then, we minimize the following phase error function to obtain optimized $a_{i,j}$ and $b_{i,j}$:

$$E(a_{i,j}, b_{i,j}) = \iint \left[1 - \frac{V_{\mathrm{ph}}}{v}\right]^2 d\tilde{k}d\theta, \quad (6)$$

where $\tilde{k} = 1/G$.

Coefficients $c_{i,j}$ and $d_{i,j}$ are also required when the absorbing boundary such as the widely used perfectly matched layer (PML) is used. Following the approach by Fan et al. (2018a), these coefficients can be determined by minimizing the error function:

$$E(c_{i,j}, d_{i,j}) = \iint (E_1^2 + E_2^2)d\tilde{k}d\theta, \quad (7)$$

where

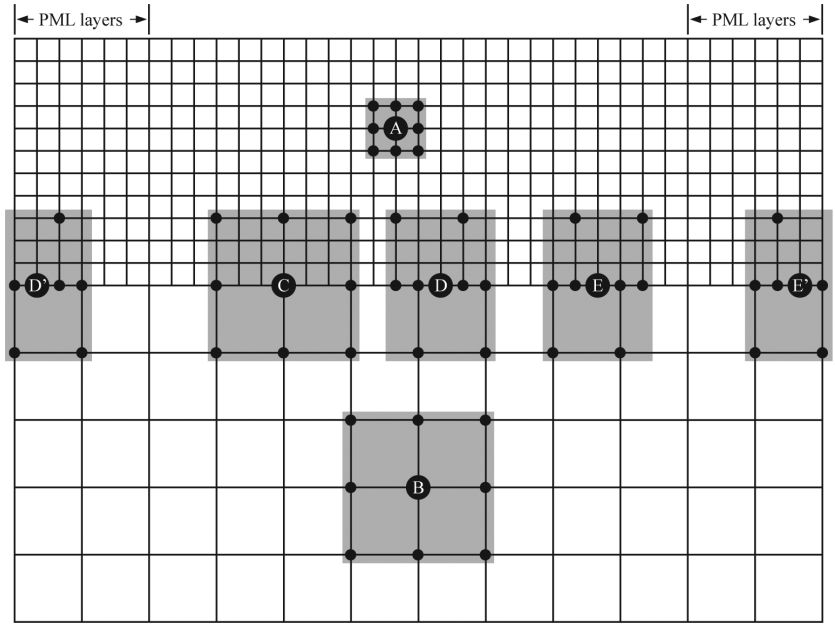

Figure 3. Nine-point discontinuous-grid configurations for $N = 3$. Grid points A and B are inside regular grids, whereas C, D, and E are located in the fine-to-coarse connecting row where special stencils are used. Different FDFD operators are designed based on the local distribution of the surrounding points. Points D′ and E′ are distorted stencils used near the absorbing boundary.

Table 1. Coefficients of the different FDFD operators in Figure 1.

Scheme	Subscripts	*b*	*c*	*d*
Stencil a	0,0	3.90288061835353E-01	−3.33338345354048E-01	−3.33327181288250E-01
	1,1	6.01878513203072E-02	2.22228445936166E-01	2.22217275204259E-01
	−2,1	2.47633081951113E-02	5.55549472878641E-02	5.55549530419119E-02
	−1,2	2.47607786492284E-02	5.55549521300179E-02	5.55549530420788E-02
Stencil b	0,0	3.45603780725254E-01	−6.19552541467508E-01	1.74940515123029E-02
	1,1	5.66108467399356E-02	6.05001067959521E-01	−2.35876546508933E-01
	1,3	1.13444490733052E-02	−9.22425195227347E-02	1.11609940505222E-01
	−1,2	5.09504376561069E-02	2.75695895762229E-02	5.33862772457136E-02
	−2,1	3.54904858053984E-02	7.92244034544985E-02	5.33862772456945E-02
Stencil c	0,0	2.71472954306941E-01	7.13688920079976E-01	−8.78812863378444E-01
	1,1	1.31797995677072E-01	−9.99646388257185E-01	8.19112363937886E-01
	3,2	4.43710985266045E-02	1.84066317080072E-01	−1.20288191535349E-01
	0,2	1.01269942034431E-02	6.81984874914736E-02	1.46294447331693E-01
	−3,1	4.22309572859399E-02	3.36926636056638E-02	3.36942436442141E-02

DOI:10.1190/geo2020-0296.1

$$E_1 = \sum_{j=0}^{N_z}\sum_{i=F(j)}^{N_x} c_{i,j}T_{i,j} \Big/ \sum_{j=0}^{N_z}\sum_{i=F(j)}^{N_x} b_{i,j}T_{i,j} + \left(\frac{2\pi \sin\theta}{G}\right)^2 \tag{8a}$$

and

$$E_2 = \sum_{j=0}^{N_z}\sum_{i=F(j)}^{N_x} d_{i,j}T_{i,j} \Big/ \sum_{j=0}^{N_z}\sum_{i=F(j)}^{N_x} b_{i,j}T_{i,j} + \left(\frac{2\pi \cos\theta}{rG}\right)^2. \tag{8b}$$

As examples, we use the above procedure to calculate optimal coefficients for three FDFD operators as shown in Figure 2. The optimized coefficients are listed in Table 1. The general features of these operators are compared in Figure 2, including the dispersion curves and structures of the impedance matrices. The structures of the matrices are related to the FDFD stencils, and they have larger bandwidths along the diagonals compared with the conventional standard nine-point operator in Jo et al. (1996). To validate the schemes, we further simulate the scalar wave propagation in a 2D homogeneous media using these schemes. Their snapshots are also shown in Figure 2. The dispersion curves of these three stencils show different accuracies, in which stencils in Figure 2a and 2b have similar accuracies because Figure 2b has only one more pair of grid points than Figure 2a and these two additional grid points stay far from the central grid point; thus, they do not affect the accuracy too much. Stencil in Figure 2c has the lowest accuracy because its grid points are more unevenly distributed and some of them stay far away from the central grid point. From Figure 2, we conclude that the accuracy of an FDFD operator is related to the shape and number of points involved in a stencil. Similar tests are conducted using other FDFD stencils, although their results are not shown here. These numerical examples demonstrate that, if more points are involved, or points are distributed more evenly, or points are closer to the central point, the resulted FD stencil tends to be more accurate.

Discontinuous-grid modeling

The subsurface velocity usually increases with the depth. To adapt to velocity variations and reduce the computation cost, a variable grid is often desirable. Fan et al. (2018a) propose a discontinuous-grid FDFD method. However, it only works for the coarse-to-fine grid spacing ratio $N = 2$, or for $N = 2^n$ by using the procedure n times, where n is a positive integer. Here, we present a general discontinuous-grid method that can be used for arbitrary integer N. In general, N can be determined by the ratio of velocities across the transition zone; e.g., we can use discontinuous grid with $N = 2$ if the velocity doubles. Considering the actual velocity contrast involved, discontinuous grids with $N = 2 - 5$ are the most useful. Because cases $N = 2$ and $N = 4$ have been covered by Fan et al. (2018a), here we only discuss cases $N = 3$ and $N = 5$, although the current procedure can be applied to an arbitrary integer N.

Because the standard nine-point operator is one of the most widely used FDFD schemes, we take it as the example to demonstrate the discontinuous-grid FDFD modeling. We first present the methodology for the discontinuous-grid scheme with $N = 3$ shown in Figure 3. Assuming that the model has lower and higher velocities in the shallow and deep areas, and the higher speed is at least three times of the lower speed, we grid the model by Δx and Δz in the upper part and $3\Delta x$ and $3\Delta z$ in the lower part. The fine grid

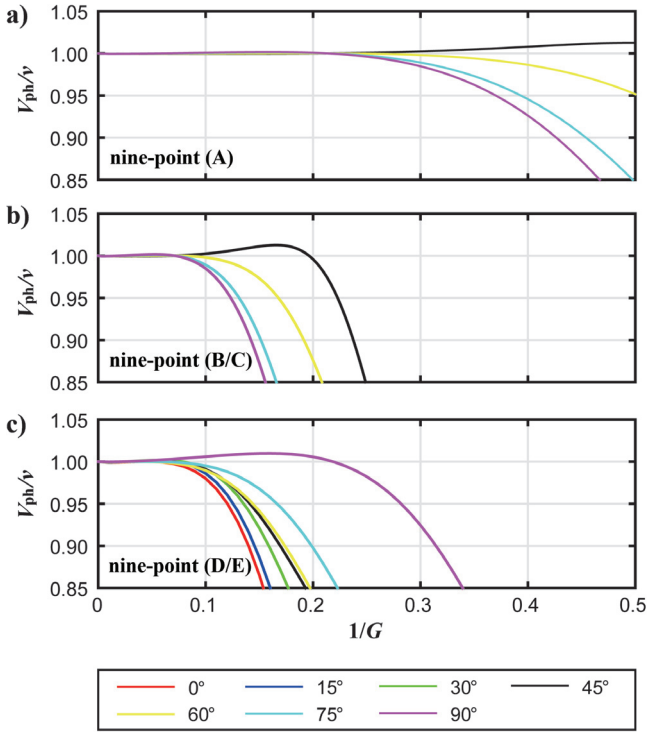

Figure 4. Normalized phase velocity curves for three types of FDFD operators in Figure 3, with standard nine-point operators at grid points (a) A and (b) B/C and (c) a new nine-point operator at grid point D/E, respectively.

Table 2. Coefficients of FD operator for the discontinuous-grid scheme with $N = 3$.

Scheme	Subscripts	b	c	d
Nine-point (D)	0,0	2.86957420011575E-01	2.35557169714165E+00	−2.74851982133288E+00
	1,0	1.22436783030788E-01	−3.58366514844076E+00	3.70056947574663E+00
	2,0	1.05931117713454E-03	1.21282254201398E+00	−1.04764309816071E+00
	2,3	3.58729260389506E-02	−2.08171046934734E-02	5.77883662163354E-02
	−1,3	5.36735597415521E-02	3.60880139786013E-02	3.78050775306212E-02

should cover the entire low-velocity area and extend into the high-velocity area for at least $3\Delta z$ to ensure the accuracy of the wavefield crossing the transition zone. If other stencils are used, the size of the overlapped zone may be different. For example, for the 25-point stencil, the overlapped zone should be at least $6\Delta z$. Figure 3 shows several typical FDFD stencils involved in the fine-grid, coarse-grid, and transition areas. In regular-grid areas including fine and coarse grids, standard nine-point operators are used, as illustrated by grid points A and B in Figure 3, and in the connecting row, FDFD operators with special stencils are used to ensure wavefield continuity across that row. The connecting row involves three kinds of grid points. One is grid point C, in which the standard nine-point operator works. The other two are grid points D and E, in which new nine-point operators are designed based on the distribution of surrounding points. The FDFD stencils at D and E are mirrored about the vertical line; therefore, we only need to calculate the optimal coefficients for one of them.

When the FD stencil reaches the absorbing boundary, the requirement of rotational symmetry around the central point may not be satisfied. Under this circumstance, we omit the grid points outside the boundary and we use distorted stencils such as D′ and E′ as shown in Figure 3. For simplicity, their optimal coefficients are still determined using the full stencils D and E. Numerical tests verified that, because of the existing absorbing condition, the wavefield is very weak when bouncing back from the boundary. Therefore, this simple boundary treatment does not affect the result too much and a high-accuracy wavefield can still be achieved.

The coefficients for FDFD schemes at D or E can be obtained following the optimization procedure in the previous section. The range of $\tilde{k}$ is set within [0, 0.08] by the trade-off between the minimum G and the phase velocity error. Table 2 lists the resulting optimal coefficients of the nine-point operator at D/E. Figure 4 shows the normalized phase velocities (the dispersion curves) for all FDFD operators in Figure 3. Taking the commonly used 1% criterion for the minimum G, i.e., keeping the threshold of normalized phase velocity at 0.99, we find that the maximum values of $1/G$ for operators at grid points A, B/C, and D/E are 0.29, 0.097, and 0.1, respectively. However, operators B-E fall into regions where the speed is at least three times faster (i.e., the wavelength is at least three times longer), the maximum values of $1/G$ are actually 0.29, 0.29, and 0.3. Therefore, for the nine-point discontinuous-grid scheme with $N = 3$, G should be at least 3.44 to limit the phase velocity error within 1%.

Similarly, we consider the discontinuous-grid scheme with $N = 5$, where the high speed in the lower area is at least $5.0 \times$ the low speed in the upper area. Figure 5 shows several typical FDFD stencils used in the fine grid, coarse grid, and transition areas. We

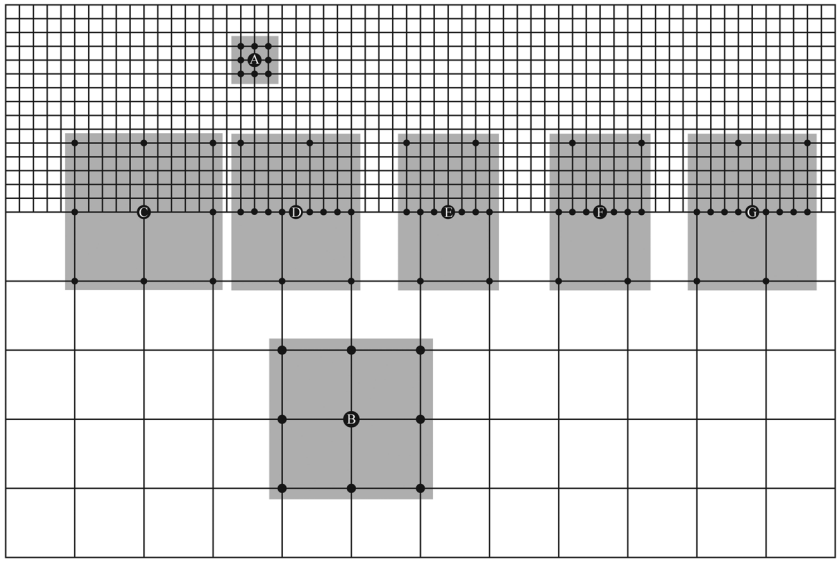

Figure 5. Nine-point discontinuous-grid configurations for N = 5.

Table 3. Coefficients of different FD operators for the discontinuous-grid scheme with N = 5.

Scheme	Subscripts	b	c	d
13-point (D)	0,0	3.30801172581863E-01	−1.46449404683130E+01	1.28177804580952E+01
	1,0	5.40766669021975E-02	1.18098310034799E+01	−9.57083469674555E+00
	2,0	1.47182388732782E-02	1.19412687302919E+01	−1.24281340417920E+01
	3,0	6.21392605255826E-03	−1.25171268933577E+01	1.25192746669509E+01
	4,0	3.18983515785329E-03	3.40504607255770E+00	−3.37204869162245E+00
	4,5	1.86478272348038E-02	−9.68831894133851E-03	1.77110195059905E-02
	−1,5	7.23523331974456E-02	1.56098742825231E-02	1.62512856079420E-02
11-point (E)	0,0	2.15067399330285E-02	1.47859279378520E+00	−1.03806199252442E+00
	1,0	3.31646837344718E-01	−1.15992722777486E+00	4.81441476592049E-01
	2,0	5.37620960493052E-02	−1.05831894116812E+00	1.12712286761476E+00
	3,0	1.90702626412470E-03	7.34627480869129E-01	−6.05374242893415E-01
	3,5	3.97511857780061E-02	−6.62997850202567E-03	2.25957127090468E-02
	−2,5	5.14261146308175E-02	1.16558727906816E-02	1.22761785019782E-02

use standard nine-point operators in the regular grid areas. In the connecting row, there are five different FDFD operators (Figure 5). The first one is the grid point located at the continuous vertical grid line (indicated by C) where the standard 9-point operator can work. The other two types are the grid points located at the discontinuous vertical grid lines (indicated by D and G), where two symmetrical 13-point schemes are used. The last two are the grid points located at the discontinuous vertical grid lines (indicated by E and F), where two symmetrical 11-point schemes are used.

The coefficients for the FDFD operators at D/G and E/F can also be calculated by optimizing the objective functions 6 and 7. The range of $\tilde{k}$ is set within [0, 0.05], and Table 3 lists the resulting coefficients. Figure 6 shows the normalized phase velocities for all FDFD operators in Figure 5. Similarly, we find that the maximum values of $1/G$ within 1% phase velocity error for operators in Figure 6a–6d are 0.29, 0.058, 0.06, and 0.06, respectively. Because operators B-G fall into the high-speed area, the maximum values of $1/G$ are actually 0.29, 0.29, 0.30, and 0.30, respectively. So for the nine-point discontinuous-grid scheme with $N = 5$, the G value should be larger than 3.44 to limit the phase velocity error within 1%.

The FDFD forward modeling is calculated by solving the linear system $AU = S$, where A is the impedance matrix, U is the wavefield, and S is the source. The size and sparsity of the impedance matrix A primarily determine the computational efficiency (Štekl and Pratt, 1998). As an example, we use a simple model to compare the impedance matrices of the uniform and discontinuous grids with $N = 3$ and $N = 5$. The model is partitioned in three ways: a uniform grid composed of 31 × 21 grid points (Figure 7a), a $N = 3$ discontinuous grid consisting of 31 × 6 grid points in the top layer and 11 × 5 grid points in the bottom layer (Figure 7c), and another $N = 5$ discontinuous grid consisting of 31 × 6 grid points in the top layer and 7 × 3 grid points in the bottom layer (Figure 7e). The structures of their impedance matrices are compared in Figure 7b, 7d, and 7f. Compared to the uniform grid, the discontinuous grid reduces the size of the impedance matrix to 37% for $N = 3$ and 32% for $N = 5$; reduces the nonzero elements to 36% for $N = 3$ and 32% for $N = 5$, respectively. For both discontinuous-grid schemes, the size and sparsity of the impedance matrix are greatly reduced.

In general, with the methodology presented above, we can build a discontinuous-grid FDFD scheme with an arbitrary N. What we should do is design accurate FDFD stencils in the fine-to-coarse connecting region according to the distribution of the surrounding grid points, followed by using the above-mentioned method to optimize the expansion coefficients and examine their accuracy. The resulting FDFD schemes can reduce the computation cost while maintaining the required accuracy.

NUMERICAL EXAMPLES

In this section, we present three numerical experiments to test the proposed discontinuous-grid FDFD scheme. We implement these simulations using one complex and two simple models. Comparisons between different results, including snapshots and waveforms obtained by our schemes and the traditional uniform-grid scheme, are used to demonstrate the accuracy and efficiency of the proposed scheme.

We first validate the discontinuous-grid FDFD scheme with $N = 3$ using a two-layer model. The model has a size of 1200 × 1200 m and velocities of 1000 and 3000 m/s in the top and bottom layers, respectively. The velocity interface is at $z = 575$ m. A 30 Hz Ricker wavelet source is used in this and the following examples, and it is injected at (600, 400) m (indicated by the red stars in Figure 8a and 8b). The uniform-grid scheme and discontinuous-grid schemes are used in the simulation. The former uses a small spatial interval of $\Delta x = \Delta z = 2.5$ m to discretize the entire model and results in a grid size of 481 × 481. The latter uses a small spatial interval of $\Delta x = \Delta z = 2.5$ m to discretize the upper area above $z = 600$ m (indicated by a dashed line in Figure 8b) to guarantee that the transition grids all fall in the high-speed region. The remaining area is discretized by a large spatial interval of $3\Delta x$ and $3\Delta z$. The resulting fine- and coarse-grid points are 481 × 241 and 161 × 80, respectively. A PML absorbing boundary is used in this and the following two examples (Tang et al., 2015; Fan et al., 2017; Wang et al., 2019b). Two receivers are placed at (750, 400) and (600, 750) m, with one in the low-speed region and the other in the high-speed region (indicated by the reversed triangles in Figure 8a and 8b). The G value is 4.44 for the uniform and discontinuous schemes if we assume that the shortest wavelength is one third of the dominant wavelength of a Ricker wavelet. Simulation results are shown in Figure 8, in which wavefield snapshots (Figure 8a and 8b) are both at 0.4 s and synthetic seismograms are compared at two receivers (Figure 8d and 8e). To demon-

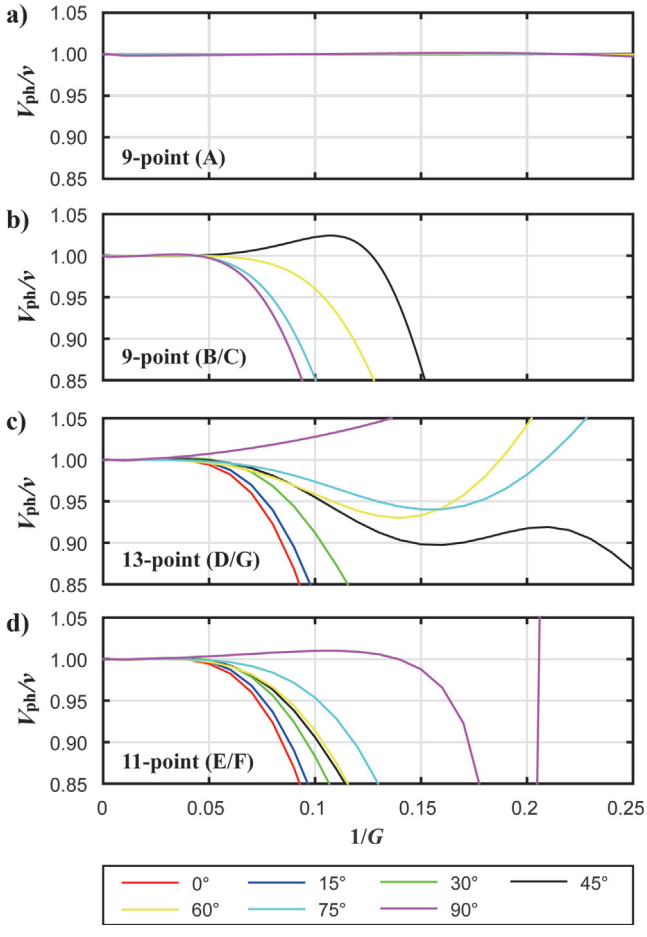

Figure 6. Normalized phase velocity curves for different FDFD operators in Figure 5, with standard 9-point operators at grid points (a) A and (b) B/C, (c) a 13-point operator at grid point D/G, and (d) an 11-point operator at grid point E/F, respectively.

DOI:10.1190/geo2020-0296.1

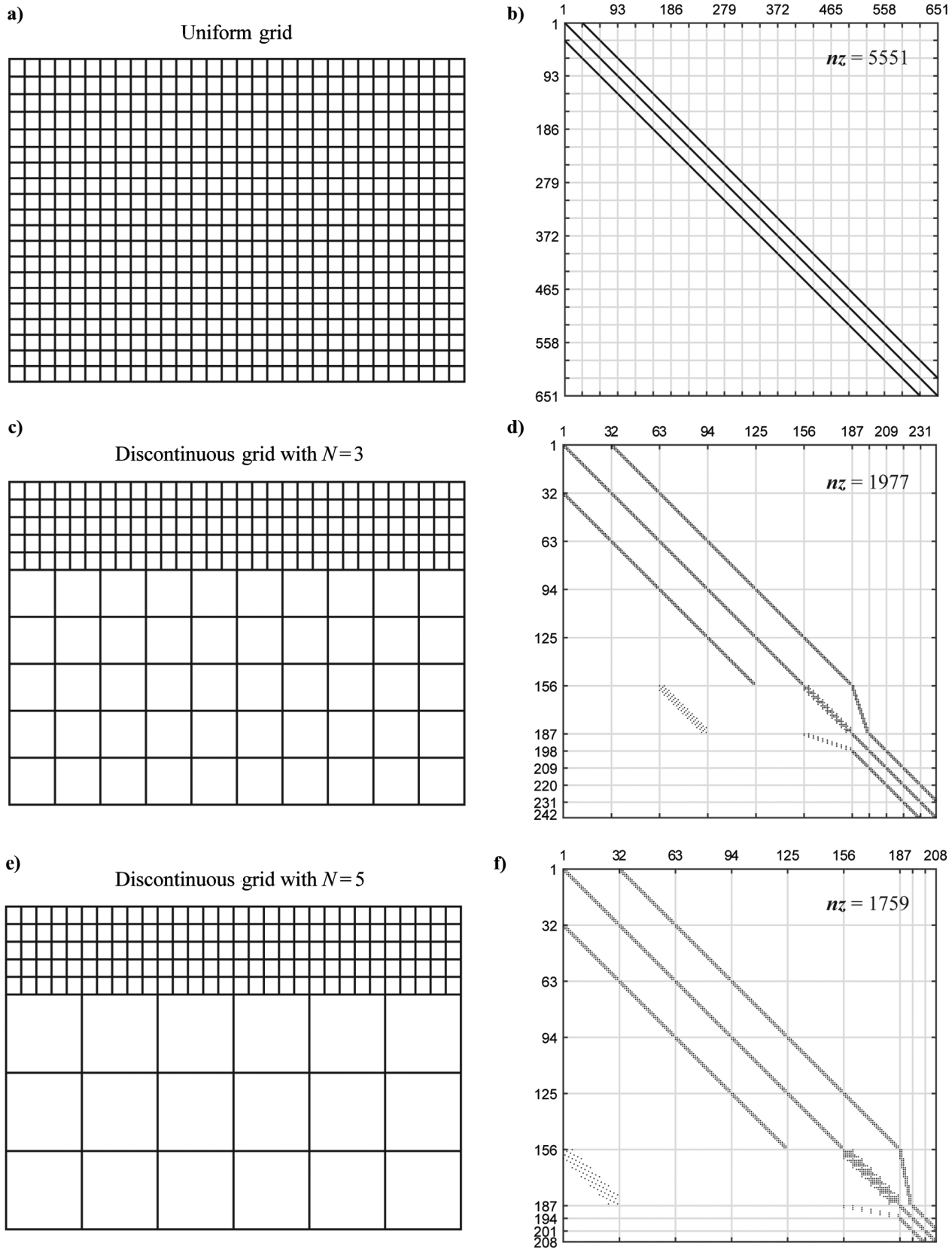

Figure 7. A velocity model discretized using (a) uniform grid, (c) $N = 3$ discontinuous grid, and (e) $N = 5$ discontinuous grid. The corresponding impedance matrices are shown in (b, d, and f), respectively. The gray areas are nonzero elements, with their numbers denoted by *nz*.

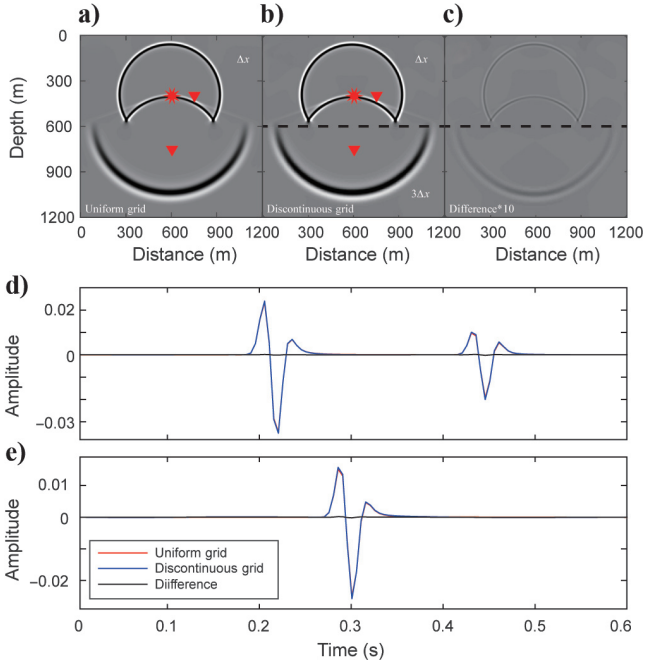

Figure 8. Comparison between the uniform- and discontinuous-grid schemes with $N = 3$. (a and b) Wavefield snapshots at 0.4 s calculated using uniform and discontinuous grids. (c) The differential wavefield amplified by 10×. The dashed line in (b) denotes the boundary between differently gridded areas. The source is denoted by a red star. (d and e) Synthetic seismograms at two receivers at (750, 400) and (600, 750) m (shown as reversed triangles in [a and b]). The red and blue traces are from the uniform- and discontinuous-grid schemes, respectively, and the black traces are their differences.

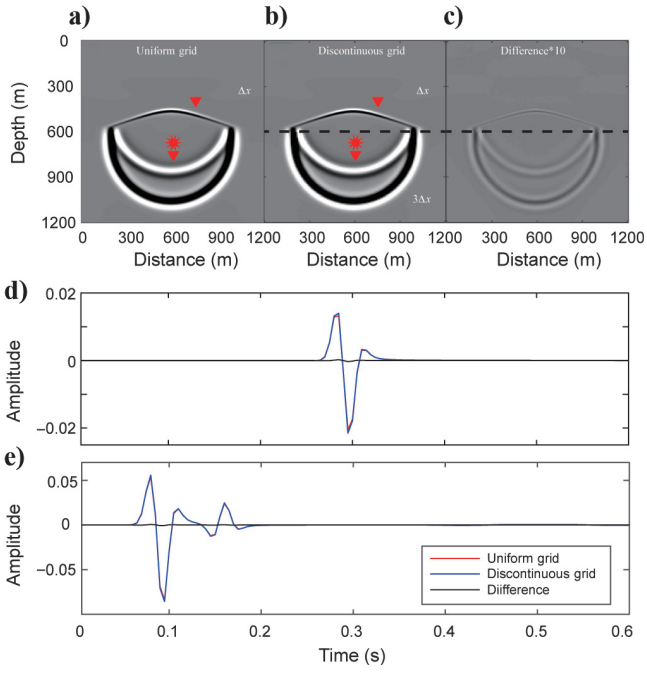

Figure 9. Similar to Figure 8 except the source is located in the high-speed layer at (600, 675) m.

strate the accuracy of the synthetic wavefield, the differential snapshot is amplified by a factor of 10 and shown in Figure 8c, and differential seismograms are overlapped in Figure 8d and 8e. The slightly polygonal-shaped waveform compared to the usual FDTD result is because they have different time sampling intervals. In FDTD, it is determined by the stability criterion, whereas in FDFD, it is determined by the sampling principle that requires two samples per period for the highest frequency. The former is usually much smaller than the latter, although they actually have the same accuracy.

To validate the case in which the source is located in the coarse-grid zone, we conduct a similar calculation by moving the source to (600, 675) m. The corresponding results are shown in Figure 9. The results in Figures 8 and 9 demonstrate that uniform and discontinuous grids generate comparable accuracy. Regarding computational costs, it is mainly dependent on the structure of the complex-valued impedance matrix due to implicitly solving the large sparse linear equations. The computational times on a single CPU 4-core (Intel Core i7-4790) desktop needed for uniform- and discontinuous-grid modelings are 774 and 229 s, respectively, because the latter reduces the number of nonzero elements and the size of the matrix to 56% for this specific numerical experiment.

We use the next two-layer model to validate the discontinuous-grid FDFD method under $N = 5$. The model has a size of 1500 × 1500 m. The velocities are 1000 and 5000 m/s in the top and bottom layers, with an interface at $z = 725$ m. The source is located at (750, 500) m. For the uniform-grid scheme, we use a small spatial interval of $\Delta x = \Delta z = 2.5$ m to discretize the entire model, and we obtain a grid size of 601 × 601. For the discontinuous-grid scheme, we use a small spatial interval of $\Delta x = \Delta z = 2.5$ m to discretize the area above $z = 750$ m (indicated by the dashed line in Figure 10b) and a large spatial interval of $5\Delta x$

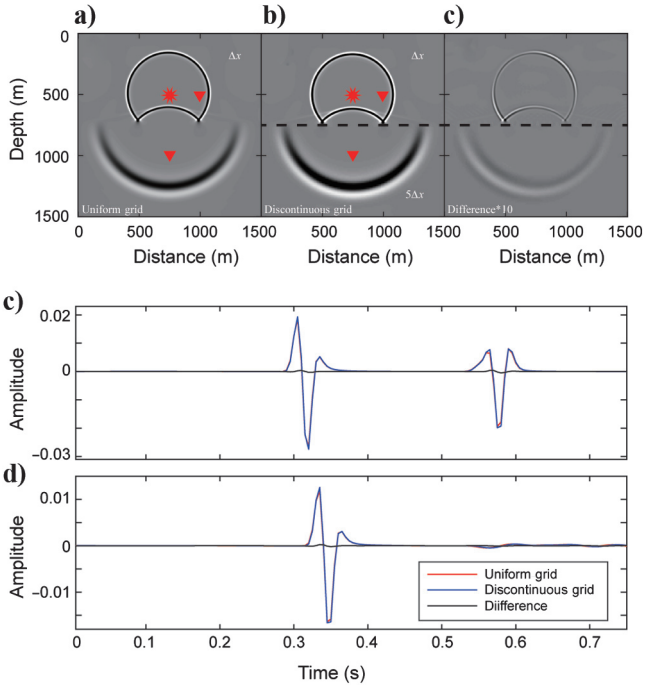

Figure 10. Comparison between the uniform- and discontinuous-grid schemes with $N = 5$. Similar to those in Figure 8, except the model velocity in the bottom layer is five times of that in the top layer.

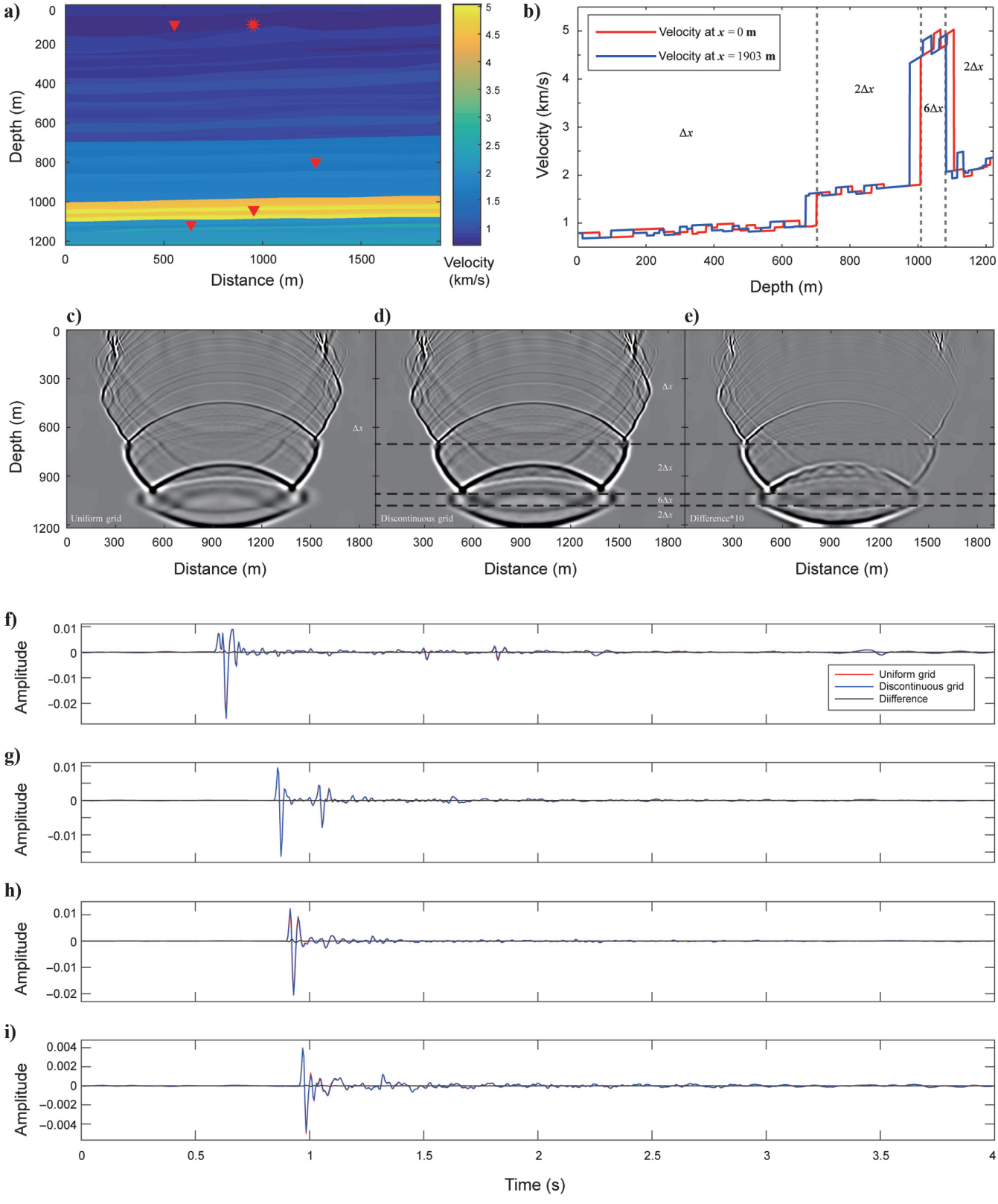

Figure 11. Simulation results in a complex velocity model using uniform- and discontinuous-grid schemes. (a) The velocity model used in the simulation. (b) The velocity versus depth at $x = 0$ and 1903 m. (c and d) Wavefield snapshots at $t = 1$ s from the uniform and discontinuous schemes, where the dashed lines in (d) denote boundaries between differently gridded areas. (e) Differential wavefield (amplified by 10 ×) between (c and d). (h-i) Synthetic seismograms calculated at locations (550, 100), (1268, 802), (954, 1038), and (634, 1120) m. The red and blue traces are from the uniform- and discontinuous-grid schemes, and the black traces are the differential waveforms.

DOI:10.1190/geo2020-0296.1

and $5\Delta z$ to discretize the remaining area. The grid points of the finely and coarsely gridded areas are 601×301 and 121×60, respectively. Two receivers are placed at (1000, 500) and (750, 1000) m, with one in the low-speed region and the other in the high-speed region (Figure 10b). Simulation results from these two different schemes are compared in Figure 10. Figure 10a and 10b compares the wavefield snapshots at 4.0 s, and shown in Figure 10c is their differential snapshot amplified by a factor of 10. Figure 10d and 10e compares the synthetic seismograms from two receivers. Regarding the computational costs, the computational times on a single CPU 4-core (Intel Core i7-4790) desktop needed for uniform- and discontinuous-grid modeling are 787 and 429 s, respectively, because the latter reduces the number of nonzero elements and the size of the impedance matrix to 52%.

In the last example, to better test the proposed discontinuous-grid method in a more realistic model having a large velocity contrast, we convert part of the Marmousi2 model using $v_P(x,z) = Cv_{P0}^2(x,z)$, where v_{P0} is the original velocity, v_P is the converted velocity, and $C = 0.25$ s/km is a constant. The resulting velocity model with a size of 1903×1220 m is shown in Figure 11a. The source and four receivers are located at (950,100), (550,100), (1268,802), (954,1038), and (634,1120) m, respectively (Figure 11a). Figure 11b shows the velocity versus depth curves at the distances $x = 0$ and $x = 1903$ m. The velocity generally increases with the depth, but there is a high-velocity salt layer close to the bottom of the model. To apply the discontinuous-grid method, we separate the entire model into four layers and use a different grid density to discretize the model. The depth ranges for these layers are 0–703, 703–1009, 1009–1081, and 1081–1220 m, with corresponding minimum velocities of 682.4, 1572.8, 4497.2, and 1930.1 m/s (Figure 11b), respectively. Based on their velocity variation ranges, we grid these regions by Δx, $2\Delta x$, $6\Delta x$, and $2\Delta x$, respectively, where $\Delta x = 1$ m. The spacing ratios at boundaries between the lower and upper layers are $N = 2$ at $z = 703$ m, $N = 3$ at $z = 1009$ m, and $N = 1/3$ (or $N = 3$ for the upper to lower layer ratio) at $z = 1081$ m.

For comparison, we also generate a set of results using the conventional uniform grid with $\Delta x = \Delta z = 1$ m. Figure 11c and 11d shows the snapshots at 1.0 s using uniform- and discontinuous-grid schemes. Figure 11e shows the differential snapshot that is amplified by a factor of 10. Figure 11f–11i compares the synthetic seismograms from four receivers located in different layers, with their differences overlapped to these waveforms. For this complex model, the discontinuous-grid modeling reduces the impedance matrix to 67%, and the computational time on a dual CPU 2×8-core (Intel Xeon E5-2630) machine from 7625 to 4856 s is compared to the corresponding uniform-grid modeling.

By comparing snapshots and synthetic seismograms in the above three numerical examples, the results demonstrated that the discontinuous-grid scheme generates highly consistent waveforms in simulating wave propagations while greatly reducing the computational cost compared to the uniform-grid scheme.

CONCLUSION

We proposed an optimal method for discontinuous-grid FDFD operators with flexible stencils. This method can be applied to the arbitrary integer coarse-to-fine spacing ratio N, given that the involved grid points are properly paired and centrosymmetric around the central point. Considering that the spacing ratio $N = 2$–5 is the most commonly encountered situation, the proposed method should be very useful in building discontinuous-grid FDFD simulations in high-contrast velocity structures for reducing the computational time and memory cost while still maintaining accuracy. To demonstrate the application of this method, we applied it to irregular FDFD stencils in connection regions with spacing ratios of $N = 3$ and $N = 5$. Many detailed procedures, e.g., designing irregular stencils, building objective functions, optimizing expansion coefficients, and analyzing dispersion curves and impedance matrices, were introduced. Numerical experiments in complex high-contrast velocity models were calculated using the discontinuous-grid FDFD optimized with the proposed method. The snapshots and waveforms calculated with these schemes have accuracies comparable to those using dense conventional uniform-grid schemes, whereas the computational costs were greatly reduced.

ACKNOWLEDGMENTS

The authors thank J. Shragge, S. Hestholm, W. Zhang, and the three anonymous reviewers for their critical comments that greatly improved this manuscript. This research is financially supported by the National Natural Science Foundation of China (grant nos. 41604037, 41630210, 41874119, and 41674107) and the Open Fund of the Cooperative Innovation Center of Unconventional Oil and Gas (Ministry of Education & Hubei Province) (no. UOG2020-09).

DATA AND MATERIALS AVAILABILITY

Data associated with this research are available and can be obtained by contacting the corresponding author.

REFERENCES

Aoi, S., and H. Fujiwara, 1999, 3D finite-difference method using discontinuous grids: Bulletin of the Seismological Society of America, **89**, 918–930.

Cao, S.-H., and J.-B. Chen, 2012, A 17-point scheme and its numerical implementation for high-accuracy modeling of frequency-domain acoustic equation: Chinese Journal of Geophysics, **55**, 239–251, doi: 10.1002/cjg2.1718.

Chen, J.-B., 2012, An average-derivative optimal scheme for frequency-domain scalar wave equation: Geophysics, **77**, no. 6, T201–T210, doi: 10.1190/geo2011-0389.1.

Chen, J.-B., and J. Cao, 2016, Modeling of frequency-domain elastic-wave equation with an average-derivative optimal method: Geophysics, **81**, no. 6, T339–T356, doi: 10.1190/geo2016-0041.1.

Chen, J.-B., and J. Cao, 2018, An average-derivative optimal scheme for modeling of the frequency-domain 3D elastic wave equation: Geophysics, **83**, no. 4, T209–T234, doi: 10.1190/geo2017-0641.1.

Chu, C., and P. L. Stoffa, 2012, Nonuniform grid implicit spatial finite difference method for acoustic wave modeling in tilted transversely isotropic media: Journal of Applied Geophysics, **76**, 44–49, doi: 10.1016/j.jappgeo.2011.09.027.

Etgen, J. T., 2007, A tutorial on optimizing time domain finite-difference schemes: "Beyond Holberg", Stanford Exploration Project Report 129, 33–43.

Falk, J., E. Tessmer, and D. Gajewski, 1996, Tube wave modeling by the finite-difference method with varying grid spacing: Pure and Applied Geophysics, **148**, 77–93, doi: 10.1007/BF00882055.

Fan, N., J.-W. Cheng, L. Qin, L.-F. Zhao, X.-B. Xie, and Z.-X. Yao, 2018b, An optimal method for frequency-domain finite-difference solution of 3D scalar wave equation: Chinese Journal of Geophysics, **61**, 1095–1108, doi: 10.6038/cjg2018L0375.

Fan, N., L.-F. Zhao, Y.-J. Gao, and Z.-X. Yao, 2015, A discontinuous collocated-grid implementation for high-order finite-difference modeling: Geophysics, **80**, no. 4, T175–T181, doi: 10.1190/geo2015-0001.1.

Fan, N., L.-F. Zhao, X.-B. Xie, X.-G. Tang, and Z.-X. Yao, 2017, A general optimal method for 2D frequency-domain finite-difference solution of

scalar wave equation: Geophysics, **82**, no. 3, T121–T132, doi: 10.1190/geo2016-0457.1.

Fan, N., L.-F. Zhao, X.-B. Xie, and Z.-X. Yao, 2018a, A discontinuous-grid finite-difference scheme for frequency-domain 2D scalar wave modeling: Geophysics, **83**, no. 4, T235–T244, doi: 10.1190/geo2017-0535.1.

Gu, B., G. Liang, and Z. Li, 2013, A 21-point finite difference scheme for 2D frequency-domain elastic wave modelling: Exploration Geophysics, **44**, 156–166, doi: 10.1071/EG12064.

Holberg, O., 1987, Computational aspects of the choice of operator and sampling interval for numerical differentiation in large-scale simulation of wave phenomena: Geophysical Prospecting, **35**, 629–655, doi: 10.1111/j.1365-2478.1987.tb00841.x.

Huang, C., and L.-G. Dong, 2009a, High-order finite-difference method in seismic wave simulation with variable grids and local time-steps: Chinese Journal of Geophysics, **52**, 176–186.

Huang, C., and L.-G. Dong, 2009b, Staggered-grid high-order finite-difference method in elastic wave simulation with variable grids and local time-steps: Chinese Journal of Geophysics, **52**, 2870–2878, doi: 10.1002/cjg2.1457.

Hustedt, B., S. Operto, and J. Virieux, 2004, Mixed-grid and staggered-grid finite-difference methods for frequency-domain acoustic wave modelling: Geophysical Journal International, **157**, 1269–1296, doi: 10.1111/j.1365-246X.2004.02289.x.

Jastram, C., and A. Behle, 1992, Acoustic modelling on a grid of vertically varying spacing: Geophysical Prospecting, **40**, 157–169, doi: 10.1111/j.1365-2478.1992.tb00369.x.

Jastram, C., and E. Tessmer, 1994, Elastic modelling on a grid with vertically varying spacing: Geophysical Prospecting, **42**, 357–370, doi: 10.1111/j.1365-2478.1994.tb00215.x.

Jo, C.-H., C. Shin, and J. H. Suh, 1996, An optimal 9-point, finite-difference, frequency-space, 2-D scalar wave extrapolator: Geophysics, **61**, 529–537, doi: 10.1190/1.1443979.

Kang, T.-S., and C.-E. Baag, 2004, Finite-difference seismic simulation combining discontinuous grids with locally variable timesteps: Bulletin of the Seismological Society of America, **94**, 207–219, doi: 10.1785/0120030080.

Kristek, J., P. Moczo, and M. Galis, 2010, Stable discontinuous staggered grid in the finite-difference modelling of seismic motion: Geophysical Journal International, **183**, 1401–1407, doi: 10.1111/j.1365-246X.2010.04775.x.

Li, A., H. Liu, Y. Yuan, T. Hu, and X. Guo, 2018, Modeling of frequency-domain elastic-wave equation with a general optimal scheme: Journal of Applied Geophysics, **159**, 1–15, doi: 10.1016/j.jappgeo.2018.07.014.

Li, Q., and X. Jia, 2018, A generalized average-derivative optimal finite-difference scheme for 2D frequency-domain acoustic-wave modeling on continuous nonuniform grids: Geophysics, **83**, no. 5, T265–T279, doi: 10.1190/geo2017-0132.1.

Liu, X., X. Yin, and G. Wu, 2014, Finite-difference modeling with variable grid-size and adaptive time-step in porous media: Earthquake Science, **27**, 169–178, doi: 10.1007/s11589-013-0055-7.

Min, D.-J., C. Shin, B.-D. Kwon, and S. Chung, 2000, Improved frequency-domain elastic wave modeling using weighted-averaging difference operators: Geophysics, **65**, 884–895, doi: 10.1190/1.1444785.

Moczo, P., 1989, Finite-difference technique for SH-waves in 2-D media using irregular grids — Application to the seismic response problem: Geophysical Journal International, **99**, 321–329, doi: 10.1111/j.1365-246X.1989.tb01691.x.

Nie, S., Y. Wang, K. Olsen, and S. Day, 2015, Stable discontinuous staggered finite difference method for elastic wave simulations: 85th Annual International Meeting, SEG, Expanded Abstracts, 3774–3778, doi: 10.1190/segam2015-5931765.1.

Oliveira, S. A. M., 2003, A fourth-order finite-difference method for the acoustic wave equation on irregular grids: Geophysics, **68**, 672–676, doi: 10.1190/1.1567237.

Operto, S., R. Brossier, L. Combe, L. Métivier, A. Ribodetti, and J. Virieux, 2014, Computationally efficient three-dimensional acoustic finite-difference frequency-domain seismic modeling in vertical transversely isotropic media with sparse direct solver: Geophysics, **79**, no. 5, T257–T275, doi: 10.1190/geo2013-0478.1.

Operto, S., J. Virieux, P. Amestoy, J.-Y. L'Excellent, L. Giraud, and H. B. H. Ali, 2007, 3D finite-difference frequency-domain modeling of visco-acoustic wave propagation using a massively parallel direct solver: A feasibility study: Geophysics, **72**, no. 5, SM195–SM211, doi: 10.1190/1.2759835.

Operto, S., J. Virieux, A. Ribodetti, and J. E. Anderson, 2009, Finite-difference frequency-domain modeling of viscoacoustic wave propagation in 2D tilted transversely isotropic (TTI) media: Geophysics, **74**, no. 5, T75–T95, doi: 10.1190/1.3157243.

Opršal, I., and J. Zahradník, 1999, Elastic finite-difference method for irregular grids: Geophysics, **64**, 240–250, doi: 10.1190/1.1444520.

Pitarka, A., 1999, 3D elastic finite-difference modeling of seismic motion using staggered grids with nonuniform spacing: Bulletin of the Seismological Society of America, **89**, 54–68.

Plessix, R.-É., 2009, Three-dimensional frequency-domain full-waveform inversion with an iterative solver: Geophysics, **74**, no. 6, WCC149–WCC157, doi: 10.1190/1.3211198.

Shin, C., and H. Sohn, 1998, A frequency-space 2-D scalar wave extrapolator using extended 25-point finite-difference operator: Geophysics, **63**, 289–296, doi: 10.1190/1.1444323.

Štekl, I., and R. G. Pratt, 1998, Accurate viscoelastic modeling by frequency-domain finite differences using rotated operators: Geophysics, **63**, 1779–1794, doi: 10.1190/1.1444472.

Tang, X., H. Liu, H. Zhang, L. Liu, and Z. Wang, 2015, An adaptable 17-point scheme for high-accuracy frequency-domain acoustic wave modeling in 2D constant density media: Geophysics, **80**, no. 6, T211–T221, doi: 10.1190/geo2014-0124.1.

Vigh, D., and E. W. Starr, 2008, Comparisons for waveform inversion, time domain or frequency domain?: 78th Annual International Meeting, SEG, Expanded Abstracts, 1890–1894, doi: 10.1190/1.3059269.

Virieux, J., and S. Operto, 2009, An overview of full-waveform inversion in exploration geophysics: Geophysics, **74**, no. 6, WCC1–WCC26, doi: 10.1190/1.3238367.

Wang, E., J. Ba, and Y. Liu, 2019a, Temporal high-order time–space domain finite-difference methods for modeling 3D acoustic wave equations on general cuboid grids: Pure Applied Geophysics, **176**, 5391–5414, doi: 10.1007/s00024-019-02277-2.

Wang, E., J. M. Carcione, J. Ba, M. Alajmi, and A. N. Qadrouh, 2019b, Nearly perfectly matched layer absorber for viscoelastic wave equations: Geophysics, **84**, no. 5, T335–T345, doi: 10.1190/geo2018-0732.1.

Wang, Y., J. Xu, and G. T. Schuster, 2001, Viscoelastic wave simulation in basins by a variable-grid finite-difference method: Bulletin of the Seismological Society of America, **91**, 1741–1749, doi: 10.1785/0120000236.

Wang, Z.-Y., J.-P. Huang, D.-J. Liu, Z.-C. Li, P. Yong, and Z.-J. Yang, 2019c, 3D variable-grid full-waveform inversion on GPU: Petroleum Science, **16**, 1001–1014, doi: 10.1007/s12182-019-00368-2.

Yang, Q., and W. Mao, 2016, Simulation of seismic wave propagation in 2-D poroelastic media using weighted-averaging finite difference stencils in the frequency–space domain: Geophysical Journal International, **208**, 148–161, doi: 10.1093/gji/ggw380.

Zhang, H., B. Zhang, B. Liu, H. Liu, and X. Shi, 2015, Frequency-space domain high-order modeling based on an average-derivative optimal method: 85th Annual International Meeting, SEG, Expanded Abstracts, 3749–3753, doi: 10.1190/segam2015-5871009.1.

Zhang, Z., W. Zhang, H. Li, and X. Chen, 2013, Stable discontinuous grid implementation for collocated-grid finite-difference seismic wave modelling: Geophysical Journal International, **192**, 1179–1188, doi: 10.1093/gji/ggs069.

Biographies and photographs of the authors are not available.